NATIONAL AERONAUTICS AND SPACE ADMINISTRATION

Technical Report 32-1383

A Comparison of Two Methods of Measuring Particle Size of Al_2O_3 Produced by a Small Rocket Motor

R. A. Dobbins
Brown University

L. D. Strand
Jet Propulsion Laboratory

JET PROPULSION LABORATORY
CALIFORNIA INSTITUTE OF TECHNOLOGY
PASADENA, CALIFORNIA
June 1, 1969

NATIONAL AERONAUTICS AND SPACE ADMINISTRATION

Technical Report 32-1383

A Comparison of Two Methods of Measuring Particle Size of Al_2O_3 Produced by a Small Rocket Motor

R. A. Dobbins
Brown University

L. D. Strand
Jet Propulsion Laboratory

JET PROPULSION LABORATORY
CALIFORNIA INSTITUTE OF TECHNOLOGY
PASADENA, CALIFORNIA

June 1, 1969

TECHNICAL REPORT 32-1383

Prepared Under Contract No. NAS 7-100
National Aeronautics and Space Administration

Preface

The work described in this report was performed by the Propulsion Division of the Jet Propulsion Laboratory. The spectrometer for this project was developed by the senior author at Brown University under Jet Propulsion Laboratory contract.

Acknowledgment

The authors are indebted to A. H. Rasmussen and C. Feldstein for assistance with the rocket firings and the instrumentation, respectively. Computer programs for data reduction and calculation of mean extinction coefficients were written by M. R. Diethelm.

Contents

Tables

Contents (contd)

Tables (contd)

Figures

Abstract

The size of the particulate effluent of rocket motors containing aluminum as a fuel additive is required in order to predict the thrust loss due to particle lag, the particulate radiant heat transfer, the particulate acoustic attenuation, particle impingement, and the plume structure and properties. A further study of the particle size of the Al_2O_3 produced by a small rocket motor as determined by tank collection and by spectrophotometric tests was performed to rationalize a previous discrepancy and to learn to use these methods in a mutually complementary fashion. Tank collection tests were performed with tank volume, aluminum loading in the propellant, and chamber pressure as the principal variables. The particle size data from tank collection tests was analyzed in the form of various mean diameters, moment ratios, and the mass median diameter. Spectrophotometric tests were performed at three wavelengths on motors with chamber pressure and aluminum content as principal variables. The tank collection tests gave internally consistent results only when the mean size was defined in terms of the low moments of the distribution function. These mean diameters show the same mild growth with chamber pressure as indicated by the optical measurements.

A Comparison of Two Methods of Measuring Particle Size of Al_2O_3 Produced by a Small Rocket Motor

I. Introduction

The importance of the particle size of aluminum oxide (Al_2O_3) produced in solid propellant rocket motors has been appreciated from the time that metallic aluminum was first used as a fuel additive. A knowledge of particle size is required in order to calculate the thrust as influenced by two-phase flow losses, particulate radiant heat transfer, particulate acoustic damping in the motor cavity, impingement of particles on nozzle entrance surfaces, and the rocket plume structure and its properties. Attempts to measure the particle size have resulted in a series of reports that describe observations differing sharply from one another, and which present contradictory conclusions. The disagreement seems to result from the normal difficulty of measuring populations of particles of widely varying sizes compounded by the extreme environmental factors present in rocket motor chamber and nozzle. In this work we are concerned with a comparison of the results of two techniques of measuring particle size with which the authors possess first hand experience. Our aim has been to gain an understanding of a marked discrepancy that was reported between the results of these two methods. We believe the present study has implications that impinge more directly upon studies conducted by others, and comment on these implications at the conclusion of this report.

The background for the present work is provided by Fig. 6 of Ref. 1 where spectrophotometric tests indicate an increase in particle size by a factor of about 1.3 while the tank tests on essentially the same motor, described in Ref. 2, show a 10-fold increase in particle size when the chamber operating pressure increases from 70 to 700 psig. The hypothesis that the growth of size with pressure indicated by the tank tests might be caused by agglomeration of the particles in the recovery tank was advanced to explain the discrepancy. Others later argued that agglomeration would occur in the rocket nozzle, and the photometric tests were unexplainable since they failed to indicate this growth. It was our belief at the outset of this study that the occurrence of particle growth in the nozzle due to varying slip velocities would indicate that the tank collection technique could prove unsatisfactory because of the shock waves and turbulent mixing that would occur within the tank at high recovery temperatures. Both shock waves and turbulence could cause further growth that might mask particle growth occurring

within the nozzle. For these reasons we planned a series of tank collection tests in which tank volume was a variable. A second series of optical tests were also performed in which spectrophotometric measurements were performed at three wavelengths of light rather than merely with two wavelengths as previously.

Our effort has been to seek an understanding of these two methods of size measurement. We consider the two methods to be potentially complementary to one another because of their distinctive capabilities. The tank collection method gives a measure of the detailed size distribution averaged over the entire duration of firing after a data-reduction process that is tedious and time consuming. The optical technique measures a well-defined mean diameter of a large number of particles leaving the rocket nozzle on a time resolved basis throughout the entire duration of the firing and involves a data reduction process that requires only seconds to perform. The difficult feature of the tank test is the sampling and analysis of the collected sample. A drawback to the optical test is its failure to yield any information about the size distribution function and the small number of large particles that are present. A major goal of our effort has been to seek to realize the potential of using both methods in a mutually complementary manner.

II. Particle Size Statistics

A complete description of the "size" of polydispersed particles is provided if the particle size distribution function is known. The size distribution function $\phi(D)$, is defined such that

$$\int_{D_1}^{D_2} \phi(D)\, dD \equiv P[D_1 < D < D_2] \tag{1}$$

where by $P\ [D_1 < D < D_2]$ we mean the probability of occurrence of size greater than D_1 and less than D_2. It is apparent that when D_1 is zero and D_2 corresponds to the largest size present, D_∞, then

$$\int_0^{D_\infty} \phi(D)\, dD = 1 \tag{2}$$

The actual number of particles in the size range D_1 to D_2 will be

$$N\,(D_1 < D < D_2) = n_o \int_{D_1}^{D_2} \phi(D)\, dD \tag{3}$$

where n_o is the total number of particles in a given population or sample from a population. Therefore

$$\phi(D) = \frac{1}{n_o}\frac{dN(D)}{dD} \approx \frac{1}{n_o}\frac{\Delta N(D)}{\Delta D} \tag{4}$$

Equation (4) in incremental form provides a convenient expression to evaluate the size distribution function when size frequency data is presented as a bar histogram.

Under certain circumstances a full description of the particle-size distribution function is unnecessary and only certain mean diameters or ratios of moments of the distribution function are required. The generalized mean diameter is commonly defined as

$$D_{PQ} \equiv \left[\frac{\int_0^{D_\infty} \phi(D)\, D^P\, dD}{\int_0^{D_\infty} \phi(D)\, D^Q\, dD}\right]^{1/P-Q} \tag{5}$$

The particular mean diameter, or ratio of moments, that is relevant is given by the detailed analysis of the particular effect of interest. For example, Rannie (Ref. 3) has analyzed the thrust loss due to particle slip when the particle velocity and thermal lags are small. If we examine his analysis [in particular, Eqs. (72) and (80) of Ref. 3] we find that under certain circumstances, the ratio of the fifth to third moment of size distribution function,

$$D_{53} = \left[\frac{\int_0^{D_\infty} \phi(D)\, D^5\, dD}{\int_0^{D_\infty} \phi(D)\, D^3\, dD}\right]^{1/2} \tag{6}$$

can be used in the theory in the form appropriate for monodispersed particles. In other words the D_{53} is the appropriate mean diameter to use in the theory for uniformly sized particles, i.e., a monodispersion, to correctly allow for the influence of the size distribution effects.

In Table 1 we display the various mean diameters or moment ratios that are pertinent to various gas-particle flow phenomena. In this study the two mean diameters that assume special importance are the D_{32}, because this size is measured by the optical technique, and the D_{30},

Table 1. Mean diameters relevant to various physical effects in gas-particle fluid mechanics and rocket technology

Gas-particle flow phenomenon	Smallest sizes	Estimated usual case	Largest sizes
Thrust loss due to particle slip, Ref. 3 (1962)	D_{53}	D_{53}	—
Optical scattering power, optical measurement of particle size, Ref. 4 (1963)	D_{63}	—	D_{32}
Acoustic dampening, Ref. 5 (1966)	D_{53}	D_{53}	D_{31}
Agglomeration due to particle lag, Ref. 6 (1967)	D_{30}	D_{30}	—

because this moment ratio enters into the theory describing agglomeration due to slip.

Another method of characterizing mean particle size involves the use of the median diameter defined as

$$\int_0^{D_m} \phi(D)\, D^i\, dD = \frac{1}{2} \int_0^{D_\infty} \phi(D)\, D^i\, dD \tag{7}$$

We will use the volume median diameter, for which $i = 3$, in order that our results may be related to other investigations. The median diameter has no theoretical usefulness except insofar as it may correlate with a relevant mean diameter.

Many different algebraic functions have been used to describe particle size distributions. We will be concerned with the log-probability function

$$\phi(D) = \frac{C_1 \exp - \left(\delta \ln \dfrac{D}{D_m}\right)^2}{D^4} \tag{8}$$

and the upper limit function proposed by Mugele and Evans (Ref. 7)

$$\phi(D) = \frac{C_2 \exp - \left(\delta \ln \dfrac{aD}{D_\infty - D}\right)^2}{D^4 (D_\infty - D)} \tag{9}$$

The constants C_1 and C_2 in Eqs. (8) and (9) are chosen so as to normalize the integrals to unity per Eq. (2). From Eq. (5) we see that it is unnecessary to evaluate the constants in calculating the mean diameters.

A wide variety of other distribution functions have been proposed, and most all of them suffer from the drawback that they fail to provide for a finite value for D_∞. The consequences of this failure were examined in detail by Mugele and Evans (Ref. 7) who have demonstrated the considerable merit to the function they have proposed.

III. Tank Collection Tests

A. Test Equipment and Procedures

A series of 30 small motor firings was conducted, using a tank collection technique, to determine whether the particle size distribution of the particulate effluent was dependent upon the size of the receiver tank. The test firings were conducted using the five different size configurations for the recovery tank described in Table 2. The test program consisted of two test firings carried out at each of three motor chamber average pressures (100, 300, and 800 psi) for each of the five tank configurations. The motor chamber pressures were adjusted by varying the nozzle throat diameter (0.970, 0.705, and 0.480 in., respectively).

In two shorter test series the effects of propellant aluminum concentration (2 and 20%) and rocket nozzle flow on the aluminum oxide exhaust particle size distribution were investigated, tank configuration No. 5 being used in all tests. In the latter series test firings were run at a motor pressure of approximately 200 psi and a tank pressure of 1 atm (with nozzle) and at an average tank pressure of approximately 200 psi both with and without the motor nozzle.

Table 2. Description of recovery tank configuration

Configuration number	Description	Length, ft	Volume, ft^3
1	Original tank	8	75
2	One-half original tank plus closure section	5.5	40
3	Original tank plus 4-ft cylindrical section	12	112
4	Original tank plus 6-ft cylindrical section	14	130
5	Original tank plus 10-ft cylindrical section	18	168

The test motor, propellant configuration, igniter system, and propellant (for a majority of the tests) were the same as used in Ref. 2, except that 30 deg converging, 15 deg diverging, conical copper nozzles with molybdenum inserts and 4/1 expansion ratios were used in the present series. The mass median diameter of the metallic aluminum added to the fuel was about 7 μm (microns). Instrumentation consisted of two Taber motor pressure gages, one Taber tank pressure gage, and an unshielded chromel-alumel thermocouple extending into the tank approximately 6 in. from the tank wall. All data was recorded on a CEC (Consolidated Electrodynamics Corp.) oscillograph recorder.

The test procedure was basically the same as that reported in Ref. 2. The head end of the motor was mounted to the inside of a 10-in. blind flange cover plate and all flanges were closed and sealed. The tank was evacuated to a pressure of 3 to 5 mm Hg and nitrogen was then introduced to attain atmospheric pressure. After a motor firing the tank was slowly vented to atmospheric pressure through a scrubber and then evacuated. The vacuum was pulled overnight to allow the inside of the tank to completely dry. Heat lamps were played on the bottom of the tank to assist in the evaporation of the liquid condensate. The following day the tank was slowly bled to atmospheric pressure, and the tank sections were separated. The walls of the tank sections were first carefully brushed to collect as much of the deposited material as reasonably possible in this manner. The tank walls were then lightly watered and scraped down with a squeegee to recover as much of the remaining material as possible. On the average, 85% of the theoretically predicted exhaust solids were recovered (60 to 105% of theoretical).

B. Sample Preparation and Electron Microscopy

For each test, the material collected by brushing was placed in a 430°F oven for 24 h to remove volatile impurities and then weighed. To break up agglomerates the material was transferred to a coarse grid Tyler screen sieve and run through a Rotab. A 4-oz sample bottle was filled with a representative sample of the recovered material and forwarded to the vendor for particle size analysis. In the following discussion this portion of the recovered material is referred to as the dry sample.

The entrained material collected in the scrubber was combined with that recovered by washing. The solid material was allowed to settle out, after which most of the acidic wash water solution was syphoned off. The settled material was transferred by washing to a 4-oz sample bottle of a known weight for particle size analysis. This portion of the recovered material is referred to as the wet sample. After analysis the wet sample (minus material analyzed) was dried and weighed.

Photomicrographs of specimens of a majority of the dry and wet samples were obtained,[1] using essentially the same electron microscopy procedure as reported in Ref. 2. For the dry samples a representative portion of each sample, obtained by a coning and quartering technique, was placed in a mild acidic electrolytic, formed with HCl and water, and dispersed with an ultrasonic vibrator. Since the wet sample was already in an acidic solution, the entire sample was dispersed ultrasonically. Aliquots of each specimen were placed on electron microscope viewing grids and dried. The grids were viewed in an electron microscope and photomicrographs made. For each sample the magnification power of the microscope was adjusted to a value such that a representative number of particles could be viewed. For each sample a minimum of four grids and photomicrographs were prepared.

C. Particle Size Analysis and Data Reduction Procedures

The particle size analysis was performed by an equivalent circle technique using a template with circular holes ranging in size from 2 to 30 mm, each including a pencil-lead thickness allowance. The holes are at 0.5 mm intervals from 2 to 10 mm and at 1 mm intervals from 10 to 30 mm. Each particle was counted according to its template hole size of best fit, as indicated by a pencil circle drawn over the particle. The restrictions placed on the particle count were:

(1) Count no particle if the periphery of that particle extends beyond the boundaries of the micrograph.

(2) Assume all particles to be spherical in character.

(3) Count no particle unless a sufficient amount of its periphery can be delineated to permit the deduction of the particle diameter.

(4) No particle below 0.1 μm need be evaluated in size but should be included in the total particle count (particles were counted down to the minimum size where individually distinguishable).

For comparison purposes particle size analyses of five of the dry samples were also performed by the commercial laboratory[2] that did the work for Ref. 2.

---

[1]Applied Space Technology (AST), Inc., Palo Alto, California.

[2]Sloan Research Industries (SRI), Inc., Santa Barbara, Calif.

For purposes of the present discussion we will use the term *parent population* to refer to the entire particulate effluent of a single firing. Most of the parent population is recovered by sweeping the tank to yield the *dry population* and by washing the tank to yield the *wet population.* Small samples of the dry population, the *dry sample,* and from the wet population, the *wet sample,* were then analyzed by electron microscopy. In this section we relate the size distribution function of the parent population to the size distribution of the dry and wet samples.

Using the subscripts d and w to designate the dry and wet population respectively, we may write, from Eq. (4)

$$\phi_d(D_i) \equiv \frac{\Delta N_d(D_i)}{n_d\,\Delta D_i} \text{ and } \phi_w(D_i) \equiv \frac{\Delta N_w(D_i)}{n_w \Delta D_i} \tag{10}$$

The total volume of material in the parent population, V_o, is the sum of the volumes in the dry and wet population

$$V_o = \frac{\pi}{6}\sum_{D_i} \Delta N_d(D_i)\, D_i^3 + \frac{\pi}{6}\sum_{D_i} \Delta N_w(D_i)\, D_i^3 \tag{11}$$

The volume fraction or mass fraction of the parent population contained in the dry population is therefore

$$f = \frac{\sum_{D_i} \Delta N_d(D_i)\, D_i^3}{\sum_{D_i} \Delta N_d(D_i)\, D_i^3 + \sum_{D_i} \Delta N_w(D_i)\, D_i^3} \tag{12}$$

But

$$\sum_{D_i} \Delta N_d(D_i)\, D_i^3 = n_d \sum_{D_i} \frac{\Delta N_d(D_i)}{n_d\,\Delta D_i}\, D_i^3\,\Delta D_i = n_d \sum_{D_i} \phi(D_i)\, D_i^3\,\Delta D_i \tag{13}$$

For P = 3 and Q = 0, Eq. (5) gives

$$(D_{30}^{(d)})^3 = \int \phi_d(D)\, D^3\, dD = \sum_{D_i} \phi_d(D_i)\, D_i^3\,\Delta D_i \tag{14}$$

Therefore from Eqs. (12–14) we find

$$f_d = \frac{n_d\,(D_{30}^{(d)})^3}{n_d\,(D_{30}^{(d)})^3 + n_w\,(D_{30}^{(w)})^3} \tag{15}$$

We also note that from Eq. (12)

$$f_d + f_w = 1 \tag{16}$$

We prepare counts of number of particles per size increment for all size increments by photomicrographic analysis of the wet sample and the dry sample. From these counts we can obtain the particle size distribution functions of the dry and wet samples

$$\phi_s(D_i) = \frac{\Delta N_s(D_i)}{n_s\,\Delta D_i} \text{ and } \phi_t(D_i) = \frac{\Delta N_t(D_i)}{n_t\,\Delta D_i} \tag{17}$$

If the dry and wet samples are statistically representative of the dry and wet populations respectively, then

$$\phi_d(D_i) = \phi_s(D_i) \text{ and } \phi_w(D_i) = \phi_t(D_i) \tag{18}$$

and also corresponding mean diameters and median diameters for the dry (wet) sample and the dry (wet) population are equal. Thus Eq. (15) can be written as

$$f_d = \frac{\frac{n_d}{n_w}\,(D_{30}^{(s)})^3}{\frac{n_d}{n_w}\,(D_{30}^{(s)})^3 + (D_{30}^{(t)})^3} \tag{19}$$

Since we know the mass fraction of the parent population contained in the dry sample, f_d, by weighing the dry and wet samples, and also the $D_{30}^{(s)}$ and $D_{30}^{(t)}$ by photomicroscopic analysis, the ratio n_d/n_w can be calculated from Eq. (19).

In view of Eq. (19) we may also write

$$\Delta N_d(D_i) = \frac{n_d}{n_s}\,\Delta N_s(D_i) \text{ and } \Delta N_w(D_i) = \frac{n_d}{n_t}\,\Delta N_t(D_i) \tag{20}$$

The number of particles of size D_i in the parent population is the sum of the corresponding quantities for the dry and wet population

$$\Delta N_o(D_i) = \frac{n_d}{n_s}\,\Delta N_s(D_i) + \frac{n_w}{n_t}\,\Delta N_t(D_i) \tag{21}$$

Thus the distribution function for the parent population is

$$\phi_o(D_i) = \frac{1}{n_s\left(1 + \dfrac{n_w}{n_d}\right)}\,\frac{\Delta N_s(D_i)}{\Delta D_i} + \frac{1}{n_t\left(1 + \dfrac{n_d}{n_w}\right)}\,\frac{\Delta N_t(D_i)}{\Delta D_i} \tag{22}$$

We solve Eq. (19) for n_d/n_w and obtain

$$\frac{n_d}{n_w} = \frac{f_d}{1 - f_d}\,\frac{(D_{30}^{(t)})^3}{(D_{30}^{(s)})^3} \tag{23}$$

Equations (22) and (23) enable us to find the size distribution function of the parent population, $\phi_o(D_i)$, in terms of the mass fraction in the dry population and the statistics of the dry and wet samples. Once we determine $\phi_o(D)$ we can determine all mean and all medium diameters from the definitions given by Eqs. (5) and (7). In the above discussion it is possible to use a variable increment size provided the same size increments are used for corresponding dry and wet samples.

D. Size Analyses of Particles Recovered From Tank Tests

The raw data was processed by means of a computer program which combined the statistics for the dry and wet samples and calculated, in addition to the distribution function of the parent population, the various mean diameters, D_{54}, D_{43}, D_{32}, D_{21}, D_{10}, D_{53}, and D_{30}, and also the volume median diameter, D_m. The total mass of the 2000 to 4000 particles counted in dry and wet samples was calculated and expressed as a fraction of the total amount of aluminum oxide produced by the motor. The small magnitude of this quantity, typically 10^{-12} to 10^{-14}, emphasizes the critical nature of the sampling procedure and the desirability of duplication of tests.

The computer program also generated quantities $\psi_1 = \ln\left(10\,\dfrac{D}{D_\infty}\right)$ and $\psi_2 = \ln\left(10\,\dfrac{D}{D_\infty - D}\right)$ as a function of the volume fraction of the parent population. The appropriateness of the log probability and the upper limit distribution functions, respectively, are revealed by plotting ψ_1 and ψ_2 against volume fraction on probability graph paper. The data usually resulted in a weakly S-shaped curve on the log probability presentation. The upper limit presentation was roughly a straight line except at the smallest sizes, where the slope of the line decreased. Many experimentally measured distribution functions deviated from these general descriptions. The upper limit distribution function was considered more satisfactory because the data points more nearly formed a straight line with this presentation. This trend supports the more detailed discussion by Mugele and Evans (Ref. 7) on the advantages of the upper limit function which they originated.

Electron microscopic analyses were performed on some of the samples by the two different subcontractors in order to test the statistical validity of the sampling and photomicrographic procedures. The data reduction of these analyses show that the high moments of the size distribution function show wide scatter when the results of one subcontractor's tests were compared with another. This is illustrated in Fig. 1, where D_{53}, D_{32}, and D_m are plotted against chamber pressure. The high scatter is caused by the occurrence of a small number of large particles that are difficult to sample properly and that totally dominate the size analysis. Thus an accurate measurement of the high moments of the distribution function or the volume median diameter, D_m, is very difficult to obtain. Lower moments of the distribution function such as D_{30}, D_{21}, and D_{10} show reduced scatter because they are less sensitive to the occurrence of one or two large particles.

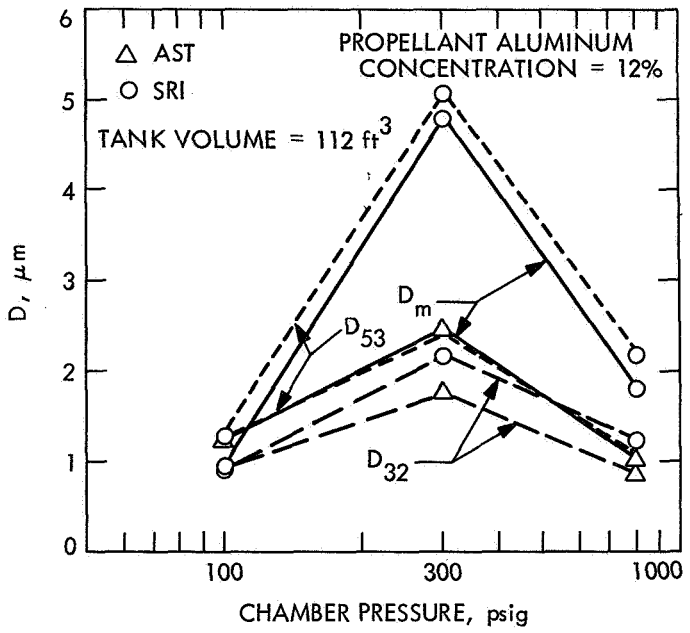

Fig. 1. Comparison of D_{53}, D_{32} and D_m measured by two subcontractors

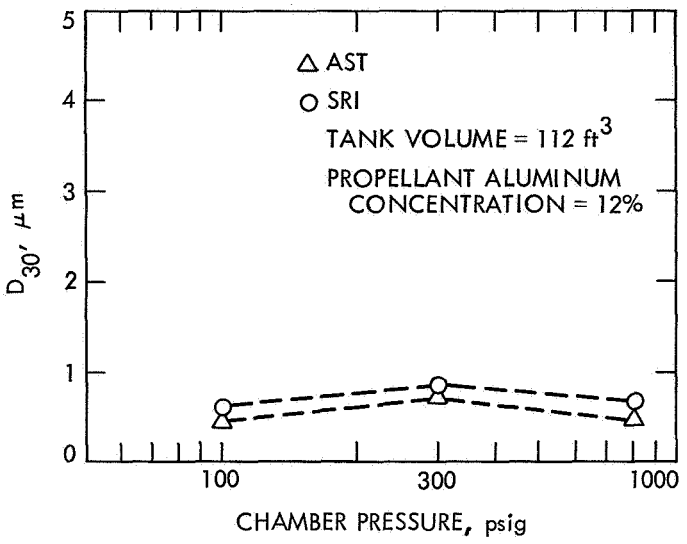

Fig. 2. Comparison of D_{30} measured by two subcontractors

In view of the generalized definition of the mean diameter D_{PQ} (Eq. 5) we find

$$D_{30} = [D_{32}\, D_{21}\, D_{10}]^{1/3} \tag{24}$$

Thus the D_{30} is a geometric average over one high moment and two low moments of the size distribution function. For this reason, and also because of the importance of this moment ratio in particle agglomeration theory, we will report primarily the D_{30} and will relate other moments to the D_{30}. A graph of the D_{30} versus chamber pressure for the same size analyses, Fig. 2, shows a substantial reduction in the scatter between the results by the two subcontractors. The D_{21} usually showed low scatter comparable to the D_{30}. The D_{10} tended to show greater scatter, apparently because of its sensitivity to the exact number of very fine particles that were counted.

The results of the series of tests conducted to determine if tank volume has an influence on the particle size is shown in Fig. 3, where D_{30} is plotted against tank volume at a constant pressure. No positive influence of tank volume on the D_{30} mean diameter is observed. The results of analysis of the data from tests in which tank size and pressure were systematically varied is depicted in Fig. 4, where D_{30} is plotted for three different tank sizes[3] at three rocket chamber pressures. These tests show no

[3]Data obtained from the two smallest tank configurations were not used because, in some instances, these earliest samples were incorrectly handled.

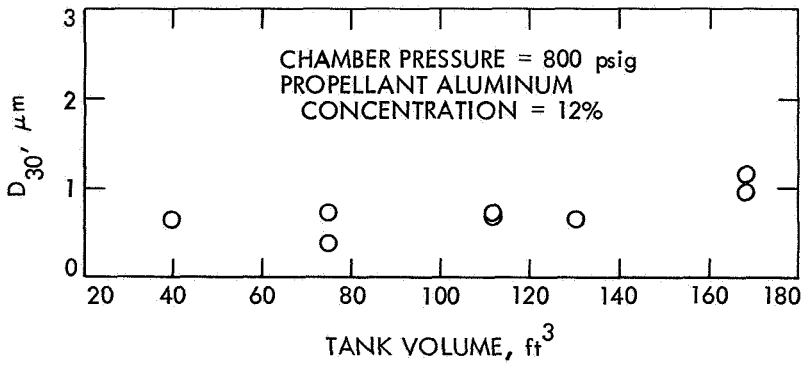

Fig. 3. Variation of D_{30} with recovery tank volume at constant pressure

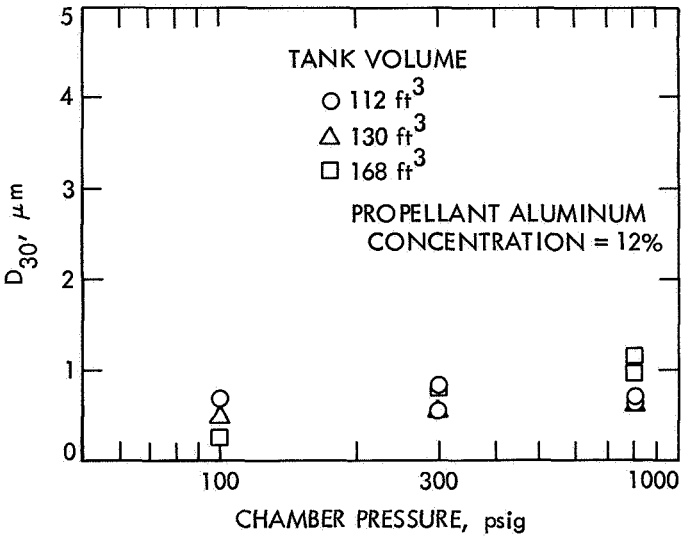

Fig. 4. Variation of D_{30} with chamber pressure and collection tank volume

systematic dependence of particle size on tank volume and show a weak dependence on chamber pressure.

The results of additional tests performed in the 168 ft³ tank are shown in Fig. 5. In the tests in which aluminum fraction was varied from 2% (three tests) to 20% (one test), shown along with the corresponding results with 12% aluminum, the scatter in the data is moderate, but no systematic variations of particle size with the aluminum loading in the propellant is noted. In the second series of additional tests the motor pressure was controlled by pre-pressurizing the tank motor assembly with nitrogen. In one case the nozzle was removed. The results of these two single firings are also plotted on Fig. 5. They show high scatter and are considered inconclusive.

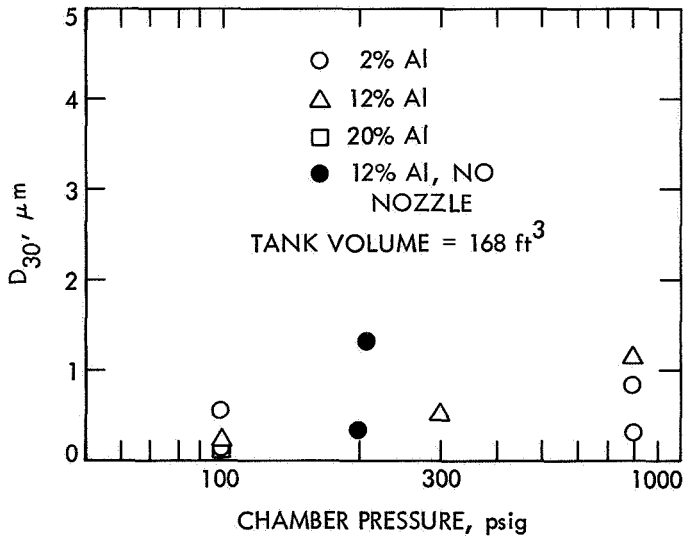

Fig. 5. Variation of D_{30} with aluminum loading and chamber pressure

We conclude from the tank tests that particle size is not sensitive to the volume of the collection tank, is not influenced by the aluminum loading in the propellant, and is weakly influenced by chamber pressure.

E. Chemical Analysis of Recovered Material

A limited chemical analysis was made of the material recovered from the tank, which was a grey-green powder. Electron diffraction measurements were performed which indicated that the smallest particles were mainly γ–Al_2O_3 and the largest particles were principally α–Al_2O_3. These observations are in agreement with measurements of refractive index (see below). The recovered material was analyzed for carbon by oxidation and gas chromatography. The average carbon content for several samples, each from the effluent recovered from the rocket motor with varying propellant fraction of aluminum were as follows: 20% Al, 0.11% C; 12% Al, 0.18% C; 2% Al, 0.57% C. The discoloration of the material from the white appearance displayed by pure powdered Al_2O_3 suggests that impurities originating in the combustion process are present. Examination of the material by optical microscopy indicated that many particles possess an orange cast and that a few of the particles contained an opaque core – possibly composed of metallic aluminum. These observations suggest to us that the imaginary portion of the refractive index for the particulate effluent from rocket motors may be substantially different from the low values applicable to pure Al_2O_3.

IV. Spectrophotometric Tests

During the present investigation we have performed additional spectrophotometric tests using the emission-scattering photometer. The theory and operation of this device have been described in Ref. 1 and the references therein. This photometer was modified by the inclusion of an additional monochromator in place of the unit previously noted as a filter and IR detector (Fig. 2 of Ref. 1). The signal from this detector was amplified and recorded in the same manner as the other two signals. Table 3 summarizes the information on wavelengths and bandpass width for the three channels of the spectrophotometer.

Table 3. Description of spectrophotometer channels

Channel no.	Wavelength, μm	Bandpass, μm	Transducer
1	0.365	0.005	Type 1P21 photomultiplier
2	1.01	0.020	Type 7102 photomultiplier
3	2.35	0.040	Type N-2 lead sulphide cell

The refractive index of the particulate effluent of the rocket motor is required in order to allow an interpretation of the spectrophotometric tests. For this reason the refractive index of the effluent material was measured by the immersion method (Ref. 8) using a 400 × optical microscope. The refractive index at $\lambda = 0.59$ μm varied systematically over the range from 1.744 to 1.665 as particle size decreased. This result is in agreement with the observations by electron diffraction pattern that indicate a larger fraction of γ–Al_2O_3 as particle size decreases. We consider that a mean value of $m = 1.71$ at $\lambda = 0.59$ μm for the cold particulate effluent is a reasonable value. We estimate the refractive index at the various wavelengths as follows. The refractive index of pure sapphire (Ref. 9) at $\lambda = 0.59$ is 1.75, or 0.05 greater than the particulate effluent. We arbitrarily apply the −0.05 correction to the refractive index of pure sapphire. Gryvnak and Burch (Ref. 10) have estimated, from experimental observations, the change in refractive index of sapphire to be +0.05 when temperature is increased from 25 to 1700°C. This temperature is reasonably representative of the temperature of the particles at the rocket nozzle exit plane where the observations of size are made. Thus our estimate is that values for the real part of the refractive index of sapphire are, fortuitously, the values applicable to the particulate effluent at the nozzle exit plane and in the near plume. These results are summarized in Table 4.

Table 4. Real part of refractive index of particulate effluent

Wavelength, μm	0.365	0.59	1.01	2.35
Pure Al_2O_3 (9)	1.80	1.76	1.76	1.73
Rocket effluent (measured)	—	1.71	—	—
Estimated for rocket effluent at various λs	1.75	—	1.71	1.68
Temperature correction (10)	+0.05	—	+0.05	+0.05
Final estimate for rocket effluent at high temperatures	1.80		1.76	1.73

The estimates of absorption coefficient of pure aluminum oxide given by Gryvnak and Burch indicate that the imaginary portion of the refractive index is on the order of 10^{-6}. However, our expectation is that the refractive index of the particulate effluent is dominated by the impurity content that is responsible for its strong coloration. We will investigate the influence of a finite imaginary portion of the refractive index later, but temporarily assume it to be zero.

The data on optical transmission of the rocket plume is analyzed by the following procedure. The spectral transmission equation for polydispersed particles can be expressed (Ref. 1) as

$$\ln t_{\lambda_i}^{-1} = \frac{3}{2} \frac{<K_i> c_v l}{D_{32}} \tag{25}$$

where c_v is the volume of particles per unit volume of gas, l is the optical path length, and the mean extinction coefficient $<K>$ is given by

$$<K_i> = \frac{\int_0^{D_\infty} K\left(\frac{\pi D}{\lambda_i}, m\right) \phi(D)\, D^2\, dD}{\int_0^{D_\infty} \phi(D)\, D^2\, dD} \tag{26}$$

where m is the (complex) refractive index and is in general a function of λ_i, the wavelength of light. The values of $<K_i>$ are calculated using the upper limit size distribution function given by Eq. (9). If we divide the transmission equations for two different wavelengths, λ_i and λ_j, by one another we find

$$\frac{<K_i>}{<K_j>} = \frac{\ln t_i^{-1}}{\ln t_j^{-1}} \tag{27}$$

From calculations of mean extinction coefficients we find the ratio $\frac{<K_i>}{<K_j>}$ is, under certain circumstances, uniquely related to D_{32} for given λ_i and λ_j and corresponding values of m. Thus optical transmission conducted simultaneously at two suitable chosen wavelengths of light can be related to the D_{32}.

The purpose of adding the third channel to the spectrophotometer was to determine if the various combinations of transmission data indicated a consistent particle size. The optical tests were conducted with the same

propellant composition, configuration, and rocket motor as was used in the tank firings. Good data was obtained in all but two of the 28 test firings. The tests included a repetition of some of the previous tests (Ref. 1) and also a series in which the aluminum loading in the propellant was varied.

The linearity of the spectrophotometer was tested prior to each run and found to be good. A series of firings indicated that the gaseous emission was negligible at 2.35 μm, although substantial at slightly longer wavelengths. The optical transmission of the plume at the exit plane of the motor was typically 95% for propellants without aluminum.

The position of the spectrophotometer with respect to the rocket motor was varied during these tests as described in Ref. 1. A series of tests were conducted at several off-axis positions (see Fig. 4b, Ref. 1), all at a distance of one meter from the nozzle exit plane, with the chamber pressure held nearly constant in the range of 705 to 725 psig. These tests showed no variation of particle size with radial position. Other tests were conducted at a nozzle station in close proximity to the nozzle exit and at a station one meter from the nozzle exit, all on the axis of the rocket motor to determine if cooling experienced by the particles and the resultant reduction in the intensity of the emitted light at the greater distance would influence the indicated size of the particles. No changes in indicated size were observed when either off-axis or on-axis position was varied. In the discussion below we do not distinguish between the various positions of the spectrophotometric beam with respect to the rocket motor axis.

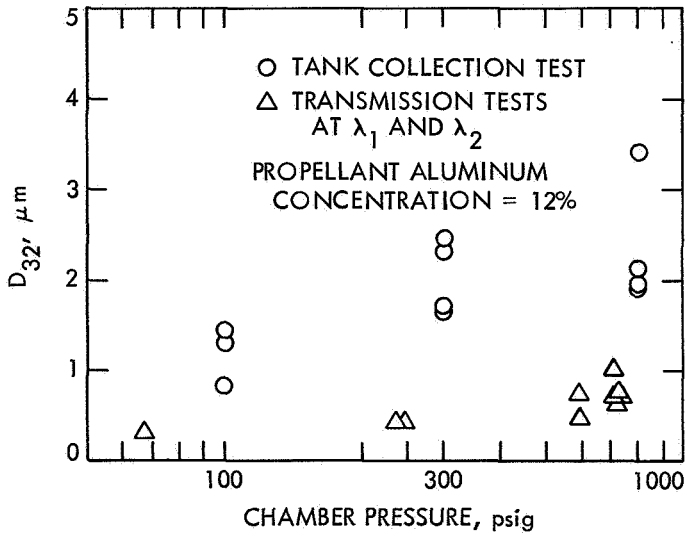

Fig. 6. Comparison of D_{32} measured by tank collection and optical transmission tests

One final preliminary point that was investigated was the influence of condensed carbon on the opacity of the plume. The most unfavorable circumstance for carbon content quoted above is when the aluminum content is lowest. Using estimates for particle size and complex refractive index of carbon available in the literature, we estimate that the optical depth, i.e., the right side of Eq. (25), was increased at most by 2% by the presence of carbon in the rocket plume, which would not influence the size measurement. The influence of carbon is even less when the aluminum loading in the propellant is increased.

Data reduction of the firings of propellants with 12% aluminum in the propellant indicated the following points:

(1) When the mean extinction coefficients, Eq. (26), were calculated with the shape parameters for the upper limit distribution function, Eq. (9), equal to the values used previously (Ref. 1), namely $a = 1.13$ and $\delta = 1.26$, the value of D_{32} indicated by tests at λ_2 and λ_3 was about 2 to 2.5 times greater than the size indicated by tests at λ_1 and λ_2.

(2) The D_{32} indicated by tests at λ_1 and λ_2 was about one-third the value of D_{32} indicated by the tank collection tests.

This comparison is shown in Fig. 6.[4]

These discrepancies were believed to be caused by a radical departure of the distribution function from its assumed form. For the shape parameters $a = 1.13$, $\delta = 1.26$ the distribution function is a skewed monomodal curve, depicted in Fig. 3 of Ref. 11.

The size distributions obtained from reduction of tank collection data showed substantially more skewness and often decreased monatonically from the smallest size increment.

[4]The reduction of the spectrophotometric data presented in Fig. 6 was accomplished with shape parameters of $a = 1.0$ and $\delta^2 = 0.50$. This data reduction gives virtually the same result for the case when $a = 1.13$ and $\delta = 1.26$ because the mean size is weakly dependent upon the shape of the size distribution function. This is the basic principle upon which the spectrophotometric method rests; it is discussed in detail in Ref. 11.

New values of the shape parameters were found by matching approximately the various ratios of mean diameters such as D_{21}/D_{30} and D_{21}/D_{10}. Ratios of low moments were preferred because these quantities were considered most accurately measured by the tank collection tests. In the first column of Table 5 we show the values of six different mean or median diameter ratios as determined by averaging the values of these numbers over ten individual tests at three pressures and three collection tank sizes. We did not observe any systematic variation of these ratios with either chamber pressure or tank size. The same ratios can be calculated for the upper limit function using expressions given by Mugele and Evans (Ref. 7) for the quantities D_{32}/D_∞, D_{31}/D_∞, D_{30}/D_∞; by noting that

$$\frac{D_m}{D_\infty} = \frac{1}{1+a} \tag{28}$$

and by using Eq. (5) to develop a relation for D_{21}/D_∞. The ratio D_{53}/D_∞ was evaluated by desk computer using Simpson's Rule. Values of $a = 0.85$ and $\delta = 0.62$ were found by trial and error to match D_{21}/D_{30} and D_{21}/D_{10} with good accuracy, although some other ratios do not match well, as is apparent by examining columns 1 and 2 of Table 5.

Table 5. Values of various ratios of mean diameters

Ratio	Experimental[a] value	Upper limit functions $a = 0.85$ $\delta = 0.62$	Truncated experimental value	Upper limit functions $a = 1$ $\delta^2 = 0.5$
$\frac{D_{53}}{D_{30}}$	5.17	3.47	2.97	3.81
$\frac{D_m}{D_{30}}$	4.66	3.40	2.57	2.454
$\frac{D_{21}}{D_{30}}$	1.13	1.18	1.10	1.11
$\frac{D_m}{D_{32}}$	1.55	1.42	1.27	1.32
$\frac{D_{21}}{D_{10}}$	3.13	3.34	2.40	2.29
$\frac{D_{32}}{D_{30}}$	3.00	2.39	2.02	1.85

[a]Average values for ten tests at three different pressures and three tank sizes. Ratios were not observed to vary systematically with tank size or pressure.

One interesting trend revealed by the data analysis was a good correlation between the median diameter D_m and the D_{53}. The ratio $D_{53}/D_m = 1.11$ for the average of the ten data points. Thus, we find that the shape of the distribution function is, fortuitously, such that the D_m and D_{53} nearly coincide. The D_m, which has been used in past studies of the size of Al_2O_3 from rocket motors, is an appropriate diameter to use to calculate thrust penalty due to gas-particle flow losses. This conclusion rests on the fulfillment of the various assumptions of Rannie's theory (Ref. 3) for the calculation of two-phase thrust penalty.

Mean extinction coefficients were calculated for the upper limit function with $a = 0.85$ and $\delta = 0.62$, Table 6, and were used to calculate the ratio of scattering coefficients as a function of particle size. Re-reduction of the spectrophotometric test data yielded: (1) roughly the same size as previously obtained by reduction of transmission tests at wavelengths λ_1 and λ_2 and (2) size at wavelengths λ_2 and λ_3 that was about 50 to 100% larger. Thus, the new information on the shape parameters did not explain the source of the discrepancy between the tank collection tests and transmission tests or internally with the transmission tests.

To understand the origin of these discrepancies we note that the observed size distributions consist of a

Table 6. Mean extinction coefficients for polydispersions obeying upper limit function (dielectric particles, $n' = 0$)

	$a = 0.85$ $\delta = 0.62$		
D_{32}, μm	$\lambda_1 = 0.365$ μm $m = 1.80$	$\lambda_2 = 1.01$ μm $m = 1.76$	$\lambda_3 = 2.35$ μm $m = 1.73$
0.20	2.171	0.2745	0.009655
0.40	2.558	1.550	0.1467
0.60	2.605	2.202	0.5847
0.80	2.595	2.350	1.140
1.00	2.564	2.485	1.633
	$a = 1.00$ $\delta^2 = 0.50$		
0.20	2.289	0.2348	0.008060
0.40	2.727	1.510	0.1252
0.60	2.728	2.336	0.5170
0.80	2.661	2.560	1.0682
1.00	2.610	2.669	1.6030

continuous function in the small sizes (the small-size continuum) and a relatively small number of large particles (the large-size discrete spectrum). The theory of the optical measurement of mean particle size is based on the existence of a continuum spectrum. Therefore, this theory must be re-evaluated to consider the large-size discrete spectrum. We consider a size distribution made up of a continuum and a single discrete line as depicted in Fig. 7. The D_{32} of the overall size spectrum can be expressed as

$$D_{32} = D_{32}^{(c)} \frac{1 + \dfrac{c_v^{(d)}}{c_v^{(c)}}}{1 + \dfrac{c_v^{(d)}}{c_v^{(c)}} \dfrac{D_{32}^{(c)}}{D^{(d)}}} \tag{29}$$

where superscript c refers to the continuous spectrum and d refers to the discrete spectrum. The transmission law for the size distribution shown in Fig. 7 may be expressed as

$$\ln \frac{F_o}{F} = \frac{3}{2} \frac{c_v^{(c)} <K^{(c)}> l}{D_{32}^{(c)}} \left[1 + \frac{c_v^{(d)}}{c_v^{(c)}} \frac{\dfrac{<K^{(d)}>}{D_{32}^{(d)}}}{\dfrac{<K^{(c)}>}{D_{32}^{(c)}}} \right] \tag{30}$$

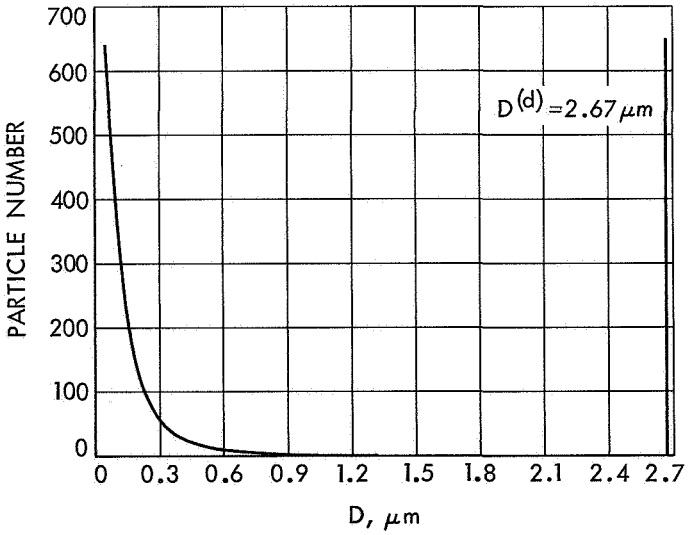

Fig. 7. A size distribution function consisting of both a small size continuum ($D_{32}^{(c)} = 0.500$) and a large size discrete spectrum ($D^{(d)} = 2.67$ μm); the continuum is an upper limit distribution with $a = 1.00$, $\delta^2 = 0.500$

where F/F_o represents the fraction of transmitted light intensity. The quantity in the square bracket on the right side of Eq. (30) represents the correction to the optical depth of the continuum size distribution and is simply $1 + \tau^{(d)}/\tau^{(c)}$, where τ denotes optical depth.

We consider two specific cases in which $D_{32}^{(c)}$ for the continuum is 0.50 μm and, with $a = 1$ and $\delta^2 = 0.50$, $D_{30}^{(c)} = 0.270$ μm and $D_{\infty}^{(c)} = 1.32$ μm. The discrete size is either 1.399 or 2.670 μm. If for every 1000 particles in the continuum there is one particle in the discrete spectrum, then we find, see Table 7, the quantity $1 + \tau^{(d)}/\tau^{(c)}$ to be nearly the same for wavelengths λ_1 and λ_2, but substantially greater at λ_3.

The ratio $<K_2/K_1>$ is scarcely influenced by the presence of the discrete spectrum and transmission tests at these wavelengths would indicate a D_{32} very nearly equal to that of the continuum only.

The explanation for this effect is that radiation at λ_1 and λ_2 are far more efficiently scattered by the continuum than by the large size discrete spectrum.

This calculation suggests that sizes indicated by transmission tests at λ_1 and λ_2 should be compared with size distribution data obtained from the tank tests which have been truncated at the end of the continuous portion of the distribution function. This procedure is somewhat tenuous because the manner in which the truncation is performed is not always clear. However, it was observed that a break in the distribution functions of samples

Table 7. Scattering power of a continuous, plus a single, discrete size spectrum[a]

λ_i	$<K_i^{(c)}>$	Case No. 1[b] $D^{(d)} = 1.399$ μm		Case No. 2[c] $D^{(d)} = 2.670$ μm	
		$K^{(d)}$	$1 + \dfrac{\tau^{(d)}}{\tau^{(c)}}$	$K^{(d)}$	$1 + \dfrac{\tau^{(d)}}{\tau^{(c)}}$
0.365	2.738	2.168	1.04	2.404	1.16
1.01	2.029	2.544	1.06	2.347	1.21
2.35	0.2803	3.076	1.55	3.510	3.26

[a] continuum — upper limit function with $a = 1$, $\delta^2 = 0.5$, $D_{32}^{(c)} = 0.50$ μm for which $D_{30}^{(c)} = 0.27$ μm. Discrete size as given. One discrete size particle per 1000 continuum particles.

[b] $c_v^{(d)}/c_v^{(c)} = 0.1338$, $D_{32} = 0.542$ μm, $D_{30} = 0.279$ μm

[c] $c_v^{(d)}/c_v^{(c)} = 0.965$, $D_{32} = 0.830$ μm, $D_{30} = 0.338$ μm

analyzed by electron microscopy typically occurred between 1.5 and 2.0 μm.

The data from the tests conducted at various pressures and the various tank sizes were recalculated after the discrete spectrum had been truncated and the ratios of mean diameters were recalculated. The values of $a = 1$ and $\delta^2 = \frac{1}{2}$ were found to generate an upper limit function that approximates the diameter ratios from the truncated data (see columns 3 and 4 in Table 5). Mean extinction coefficients were calculated for the above values of a and δ from which the D_{32} were obtained by the procedure outlined above. The D_{32} were also calculated for the truncated data and the comparison is shown in Fig. 8. The generally favorable comparison of the D_{32} given by the truncated tank collection data and the transmission tests suggests that the actual distribution does have a bimodal character. We observe that both the truncated and untruncated data display about the same fractional growth with chamber pressures.

The results may be summarized as follows. The transmission tests are explained by considering the true distribution function to possess a bimodal character. The transmission tests at wavelengths λ_1 and λ_2 are found to be of a proper selection to allow the small-size distribution to be measured. The transmission test at λ_3 is sensitive to the large sizes, which in small samples appears as discrete spectra, but would require a transmission test at a fourth suitably selected wavelength in order to permit quantitative interpretation in terms of the mean size of the large size spectrum. The truncated size distributions that presumably represents the small size continuum agree with the size indicated by the transmission tests at wavelengths λ_1 and λ_2. The transmission test data at λ_3 is not useful except as a non-quantitative, positive indication of the bimodal character of the size distribution function.

A number of optical tests were conducted with the aluminum loading in the propellant varied. We interpret this series of tests within the context of the above model. Specifically, we reduce the optical data with extinction coefficients calculated for an upper limit function for which $a = 1$, $\delta^2 = 0.50$, and we consider the size so measured to be the small size spectrum of a bimodal size distribution function. The results are shown in Fig. 9, where we find particle size is weakly influenced by aluminum loading. This is in agreement with results of tank collection tests (Fig. 5).

Finally, for this same set of shape parameters, $a = 1.00$ and $\delta^2 = 0.50$, we have calculated mean extinction coefficients for refractive indices with non-zero imaginary components (n'). The results are summarized in Table 8 for imaginary portions of the refractive index equal to 10^{-4} and 10^{-2}, such as might result from the (unknown) influence of impurities. For $n' = 10^{-2}$, or 10^{+4} greater than the value applicable for pure Al_2O_3, we find the value of $<K>$ only slightly different from its value for dielectric materials ($n' = 0$). We are therefore justified in considering the particles to be dielectric for the purpose of predicting their scattering power as a function of particle size or conversely. We expect that the emissive power of the particles will be strongly influenced by the impurities, which will control the imaginary portion of the refractive index.

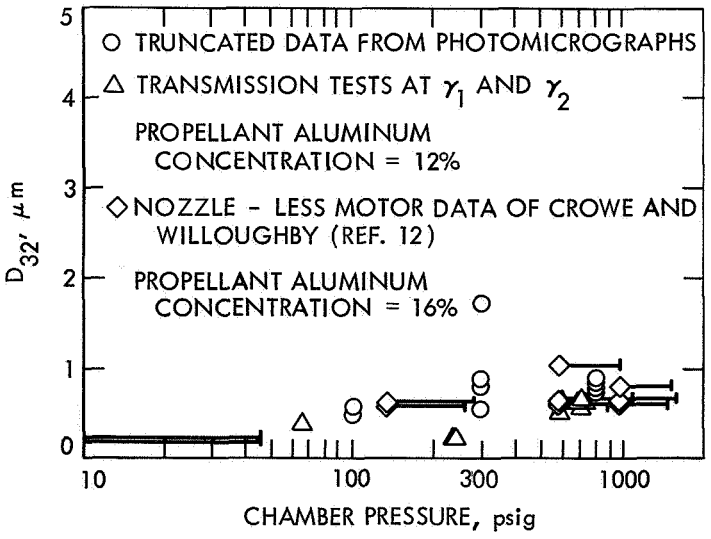

Fig. 8. Comparison of particle size measured by transmission tests at λ_1 and λ_2 with truncated photomicrographic data; data from Ref. 12 converted from D_m to D_{32} as described in text

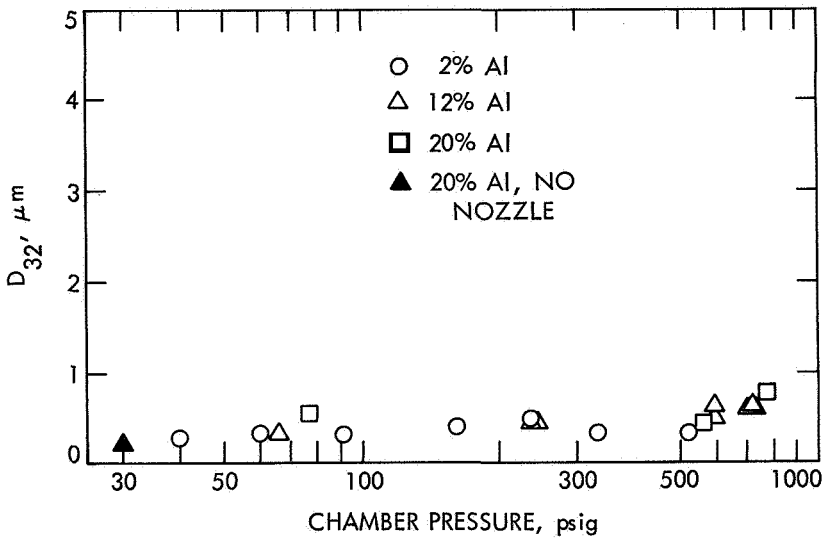

Fig. 9. Measurement of particle size (D_{32}) from transmission tests with varying aluminum content in propellant

Table 8. Mean extinction and absorption coefficients for a polydispersion obeying upper limit distribution function (nondielectric particles)

$a = 1.00$ $\delta^2 = 0.500$ ($D_{32} = 0.500$ μm)						
n'	$\lambda_1 = 0.365$ μm		$\lambda_2 = 1.01$ μm		$\lambda_3 = 2.35$ μm	
	$\langle K \rangle$	$\langle K_{abs} \rangle$	$\langle K \rangle$	$\langle K_{abs} \rangle$	$\langle K \rangle$	$\langle K_{abs} \rangle$
0	2.738	0	2.029	0	0.2803	0
10^{-4}	2.736	3.298^{-3}	2.029	8.513^{-4}	0.2804	1.976^{-4}
10^{-2}	2.728	2.435^{-1}	2.019	8.080^{-2}	0.2960	1.957^{-2}

V. Comparison of Experimental Results With Theory for Particle Agglomeration Due to Slip and Collision

The experimental results can be interpreted using the theory for agglomeration of particles due to slip and collision by Marble (Ref. 6). This theory incorporates the same mechanism of agglomeration that Crowe and Willoughby (Ref. 12) used in their computation of particle growth due to velocity lag. We use Marble's theory here because its formulation is general and can be appropriately specialized. In this analysis the linearized gas particle fluid conservation equations are used to predict the slip velocities for an assumed distribution of particle sizes. The particle collisions, each assumed to result in agglomeration of the colliding partners, are then calculated throughout the entire nozzle volume by employing a similarity solution. The growth of the mean particle size is then calculated as a function of a parameter that depends only on the Mach number of the local nozzle station. Some important conclusions of this analysis are that final particle size depends on the nozzle exit Mach number and is independent of the scale of the rocket motor, that growth parameter achieves 80% of its final value at the nozzle throat position, and that particle mass fraction and chamber pressure enter into the growth ratio as a product. Thus a ten-fold increase in either particle mass fraction or chamber pressure would result in the same fractional increase of particle size. In the following analysis we use the particle size distribution representative of those we have observed to calculate a theoretical value of the growth constant that is considered appropriate for the size distribution functions encountered in this work. We then compare the observed growth constant with the theoretical growth constant.

The growth constant in Marble's agglomeration theory is defined by

$$C_a = \frac{3}{2} \int_0^\infty \psi(\omega)\, d\omega \int_0^\infty \psi(\omega')\, g(\omega, \omega')\, d\omega' \qquad (31)$$

where the collision function, $g(\omega, \omega')$ is

$$g(\omega, \omega') = (\omega^{1/3} + \omega'^{1/3})^3 \left| \omega^{1/3} - \omega'^{1/3} \right| \qquad (32)^5$$

[5]Equation (32) differs from Eq. (47) of Ref. 5 by a typographical error in sign required to provide agreement with Eq. (26) of Ref. 5.

and where $\psi(\omega)$ is a transformed size distribution function. We may relate the particle size spectrum $f(m)$ used by Marble to the size distribution function $\phi(D)$, defined herein by formulating the expression for the mass of particles per unit volume of space in terms of both functions

$$\int_{m=0}^{\infty} m\, f(m)\, dm = \frac{\pi}{6}\, n\, \rho_P \int_{D=0}^{\infty} \phi(D)\, D^3\, dD \tag{33}$$

where $m = \frac{\pi}{6}\, \rho_P\, D^3$ and n = number of particles of all sizes per unit volume. From the above relation we find

$$f(m) = \frac{2n}{\pi\, \rho_P}\, \frac{\phi(D)}{D^2} \tag{34}$$

From Marble's Eqs. (24), (37), and (39) we find $f(m)$ and $\psi(\omega)$ related by

$$f(m) = \frac{\rho}{\rho_c}\, \frac{n_c}{m_c}\, \frac{1}{\bar{\xi}^2}\, \psi(\omega) \tag{35}$$

where

m_c is the average mass of particles in the chamber,

n_c is the number of particles per unit volume in the chamber,

ρ is the gas density at local nozzle station,

ρ_c is the gas density in rocket chamber,

$\bar{\xi}$ is the ratio of local mean particle mass to its initial value in the chamber and

ω is the mass of the particle made dimensionless with respect to local average particle mass.

In view of Eq. (34) and (35), the relationship between the three forms of the size distribution function can be expressed as

$$f(m) \sim \psi(\omega) \sim \phi(D)/D^2 \text{ and } m \sim \omega \sim D^3 \tag{36}$$

The average mass of the particles in the chamber is

$$m_c = \left[\frac{\int_0^{\infty} m\, f(m)\, dm}{\int_0^{\infty} f(m)\, dm} \right]_c \tag{37}$$

By inserting Eq. (34) into Eq. (37) and converting the integration variable to diameter we find

$$m_c = \frac{\pi}{6}\, \rho_P\, (D_{30})_c^3 \tag{38}$$

Thus mass average diameter m_c corresponds to $(D_{30})_c^3$ as defined earlier. From Marble's Eqs. (23), (24), and (32) we find

$$\bar{\xi} = \left[\frac{\int_0^{\infty} f(m)\, dm}{\int_0^{\infty} m\, f(m)\, dm} \right]_c \frac{\int_0^{\infty} m\, f(m)\, dm}{\int_0^{\infty} f(m)\, dm} \tag{39}$$

By combining Eqs. (37–39) we have

$$\frac{D_{30}}{(D_{30})_c} = (\bar{\xi})^{-1/3} \tag{40}$$

Finally, when $\bar{\xi}$ is evaluated, the growth ratio is given as

$$\frac{D_{30}}{(D_{30})_c} = \left[1 - \frac{C_a}{12}\, \frac{\rho_c\, a_c\, (D_{30})_c}{\mu_c}\, \chi\, \eta \right]^{-1} \tag{41}$$

Where

a_c = sonic velocity in rocket motor (stagnation conditions),

μ_c = viscosity of gases at stagnation conditions,

ρ_c = density of gases at stagnation conditions,

χ = mass fraction of particles at stagnation conditions.

The variable η is presented graphically (Ref. 6) and is equal to unity for Mach number >1.7. Marble evaluated the growth constant, C_a, assuming $\psi(\omega) = a/\omega^4$ for $\omega \geq \omega_0$, but this calculation can be re-evaluated using the knowledge of $\phi(D)$ obtained in this study.

A plot of the calculated values of $\phi(D)$ vs D on log-log paper suggests that $\phi(D) \propto D^{-2}$ is the best integer power law form for the distribution function. We also find that a graph of $\phi(D) \propto D^{-2}$ on an upper limit distribution plot is very close to a straight line with $a = 0.406$ and $\delta = 0.768$. These values of the shape parameters a and δ are acceptable in view of the crudeness of a power law distribution function. From Eq. (34) we find

$f(m) \alpha D^{-4} \alpha m^{-4/3}$ and from Eq. (35) $\psi(\omega) \alpha \omega^{-4/3}$. We then express the power law distribution function as

$$\begin{aligned} \psi(\omega) &= a_o \omega^{-4/3} \qquad \omega_0 < \omega < \omega_\infty \\ &= 0 \qquad\qquad\quad \omega < \omega_0,\ \omega > \omega_\infty \end{aligned} \tag{42}$$

where a_o is a constant which must satisfy the normalizing Eqs. (38) and (40) of Ref. 6. By requiring these equations to be satisfied we find

$$a = \frac{1}{3\,(D_\infty/D_0 - 1)} \left[\frac{2\,(D_\infty/D_0)^2}{(D_\infty/D_0 + 1)}\right] \tag{43}$$

$$\omega_0 = \frac{2}{D_\infty/D_0\,(D_\infty/D_0 + 1)} \tag{44}$$

$$\omega_\infty = \frac{2\,(D_\infty/D_0)^2}{D_\infty/D_0 + 1} \tag{45}$$

The normalizing equations restrict the number of functions that can be used in this analysis and the fact that $\phi(D) \alpha D^{-2}$ with upper and lower limits can be applied is very fortunate. We insert Eqs. (32) and (43) into Eq. (31) for the agglomeration constant and obtain

$$C_a = \frac{3}{2} a^2 \int_{\omega_0}^{\omega_\infty} \frac{d\omega}{\omega^{4/3}} \int_{\omega_0}^{\omega_\infty} \frac{d\omega'}{\omega'^{4/3}} \left(\omega^{1/3} + \omega'^{1/3}\right) \left|\, \omega^{1/3} - \omega'^{1/3} \,\right| \tag{46}$$

The inner integral is separated into two parts to remove the absolute sign and ω and ω' are replaced by $\eta = \omega/\omega_\infty$ and $\zeta = \omega'/\omega_0$ respectively.

$$C_a = \frac{3}{2} a^2\, \omega_0^{2/3} \int_1^{\eta_\infty} \frac{d\eta}{\eta^{4/3}} \left[\int_1^{\eta} \frac{d\zeta}{\zeta^{4/3}} \left(\eta^{1/3} + \zeta^{1/3}\right)^3 \left(\eta^{1/3} - \zeta^{1/3}\right) + \int_{\eta_\infty}^{\eta} \frac{d\zeta}{\zeta^{1/3}} \left(\eta^{1/3} + \zeta^{1/3}\right)^3 \left(\eta^{1/3} - \zeta^{1/3}\right)\right] \tag{47}$$

By evaluating the two inner integrals, we find

$$C_a = \frac{3}{2} a^2\, \omega_0 \int_1^{\eta_\infty} d\eta \left[4\eta^{-1/3} \ln \eta - 14\eta^{-1/3} + 3 - 3\eta^{-1} + \eta^{-4/3} + 3\eta_\infty^{-1/3} - 2\eta^{-1/3} \ln \eta_\infty + 3\eta^{-1} \eta_\infty^{2/3} + \eta_\infty \eta^{-4/3}\right] \tag{48}$$

Evaluating the outer integral and using Eqs. (43) and (44), we find the agglomeration constant can be expressed as

$$C_a = \frac{2^{4/3}}{6} \frac{\eta_\infty^{2/9}}{(\eta_\infty^{1/3} - 1)^2\,(\eta_\infty^{1/3} + 1)^{4/3}}\, f(\eta_\infty) \tag{49}$$

where

$$\begin{aligned} f(\eta_\infty) &= \left[6\,(\eta_\infty^{2/3} + 1) \ln \eta_\infty + \eta_\infty - \eta_\infty^{-1/3} + 5\,(1 - \eta_\infty^{2/3})\right] \\ \text{and } \eta_\infty &= (D_\infty/D_o)^3 \end{aligned} \tag{50}$$

We note that when $\eta_\infty = 1$, i.e., all particles are the same size, then $f(\eta_\infty) \to 0$ and no collisions occur.

In order to find the appropriate value of η_∞ we have matched the ratio of various mean diameters. The ratio D_{30}/D_{10} was found to be useful for this purpose because this ratio is found to be reasonably sensitive to η_∞ in the case when $\phi(D) \alpha D^{-2}$. From the definition of D_{PQ} we find

$$\frac{D_{30}}{D_{10}} = \frac{\eta_\infty^{1/3} - 1}{\eta_\infty^{1/3} \ln \eta_\infty^{1/3}} \left[\frac{1}{2} \eta_\infty^{1/3}\, (\eta_\infty^{1/3} + 1)\right]^{1/3} \tag{51}$$

From Eqs. (49) and (51) we calculate the dependence of the agglomeration constant on D_{30}/D_{10}. Examination of the experimental data shown in column 1 of Table 5 indicates the value of D_{30}/D_{10} of 2.76 is appropriate. The corresponding theoretical value of C_a is found to be about 10.7.

From the experimental data given, Fig. 4, we find for 12% Al or $\chi = 0.227$ the increase in D_{30} for a pressure range of 100 to 800 psig to be about 1.72. If we assume that the entire growth is due to the velocity slip and agglomeration mechanism, then it is possible to calculate an experimental value of the agglomeration coefficient within the context of the linearized similarity solution to the agglomeration problem.

Using estimates of fluid properties at rocket chamber conditions given in Table 9, the growth factor of 1.72 for an 8-fold increase in chamber pressure, and further assuming that the size at the nozzle entrance is independent of chamber pressure, we find the experimental value of the agglomeration constant is about 6.4% of its theoretical value. It is possible that whatever mechanisms that influence particle size of Al_2O_3 within the flame front at the propellant surface or in the space between the burning surface and the propellant may in fact be responsible for the growth of size as pressure is increased. Thus, the experimental value of agglomeration theory must be considered an upper bound. As a possible explanation of the large difference between the theoretical and the experimental values of agglomeration constant we offer the following possibilities. Both Rudinger (Ref. 13) and Selberg and Nicholls (Ref. 14) have reported measured particle drag coefficients to be considerably higher than theoretical values. Rudinger recently has attributed the increase in drag to be due to the influence of the wakes of the particles on the fluid through which the particles move. Selberg and Nicholls believe roughness of the particle surface is responsible for drag augmentation. Here we point out that an increase in drag has the same effect of reducing the theoretical agglomeration coefficient proportionally. Thus, if one were to use Rudinger's high drag coefficients in Marble's theory one would conclude that no agglomeration is predicted. This theory would then also indicate no particle growth would occur in rocket motors irrespective of their size.

Table 9. Assumed thermodynamic and transport properties for rocket chamber for calculations of particle growth by agglomeration due to slip

Property	Assumed value
Combustion flame temperature	3050°K
Molecular weight of gases	25
Ratio of specific heats	1.20
Sonic velocity, a_c	$1.092 \times 10^{+5}$ cm/s
Dynamic viscosity, μ_c	9.0×10^{-4} P (poise)
Gas density @ 100 psia, ρ_c	0.75×10^{-3} gm/cm^3

An alternative possible explanation for the small value of the experimental value of the agglomeration coefficient is the possibility that coalescence of particles on contact does not always occur. It is known that the particles will avoid collisions due to the pressure distribution at small approach velocities and that they will shatter into small droplets at high approach velocities.

We can examine the sizes produced when Al fraction is varied at constant pressure to learn more of the possibility of agglomeration due to particle slip. In this case we again find very small growth when the aluminum content is varied from 2% to 20%. Thus, again we find no growth under a circumstance when a large change in growth would be expected by the mechanism of particle slip and collision.

In summary we conclude that the variation of particle size with pressure is slight and amounts to a factor of 1.72 increase for a pressure increase by a factor of 10. We find no significant growth when aluminum fraction in the propellant is increased. This evidence suggests that the growth that does occur when pressure is varied is due to mechanisms that influence the size of the particles before they reach the nozzle entrance.

In the above discussion we are comparing the low-moment ratios with a linearized theory that requires that the particles be such that slip velocities are small compared to gas velocity. It is possible that significant growth due to particle lag can occur in sizes that are too large to be described by the linearized theory. We therefore examine the D_{53}, which is very nearly equal to the D_m, to see if evidence of more extreme growth is present in the high-moment ratios. Here we find a growth factor of about 1.6 over an 8-fold pressure ratio. No systematic variation of D_{53} with aluminum loading is noted. The scatter of the data is very great, however, and we draw no conclusions on the presence or absence of growth in the high-moment ratios from our tests. The scatter is attributed to the extreme difficulty in sampling the large-size tail of the size-distribution function.

VI. Comparison of Other Investigators

The results of this study can be compared with other tank collection studies by Crowe and Willoughby (Ref. 12). They conducted an extensive series of firings into a tank

using rocket motors and propellants comparable to those used in this program. One difference in the test procedures should be noted. In this program motor chamber pressure was controlled by varying nozzle throat area; in the study by Crowe and Willoughby the nozzle throat area was fixed and the propellant surface area was varied.

Their experimental results, reported as mass median particle sizes, indicate a growth of particle size with increasing rocket chamber pressure and a lesser amount of growth when the same rocket motors were fired, with nozzle removed, into a pre-pressurized tank. These results were interpreted to indicate that particle growth due to collision and agglomeration occurred in the rocket nozzle. This conclusion is in conflict with the particle low-moment ratio results of this investigation. Another possible explanation is that the presence of the rocket nozzle provides a surface for the deposition of a liquid layer of Al_2O_3 which is subsequently shed to form large particles by the viscous shear forces of the boundary layer. Figure 10 is a photograph of the interior surface of a rocket motor end closure. Small crevices formed by aerodynamic erosion of this layer are apparent. At high aluminum loadings and small nozzle throat diameters the thickness of this layer was sufficient to cause loss of control of chamber pressure.

We advance the hypothesis that the increase in particle size, observed by Crowe and Willoughby in their tests on motors equipped with nozzles, may have been because the nozzle served as a surface on which increased deposition and erosion occurred and that the erosion of this deposited layer was the source of the large particles. This hypothesis provides a satisfactory explanation to many of the results of the present study and that of Crowe and Willoughby. The data obtained by the latter investigators in their tests without nozzles can be compared with our results for the truncated tank collection data and the spectrophotometric tests at λ_1 and λ_2. Since Crowe and Willoughby report mass median diameter we have converted their values to D_{32} by the ratio of $D_m/D_{32} = 1.27$ applicable for the truncated experimental values (see column 3 of Table 5). The results are shown in Fig. 8 and indicate quite good agreement between the three sets of observations. In addition, we can compare the untruncated data from our tank tests with the data from the tests of Crowe and Willoughby in which nozzles were used. The results are shown in Fig. 11, where again the latter data has been converted to D_{30} by using the ratio $D_m/D_{30} = 4.66$ applicable to the untruncated experimental data (see column 1 of Table 5). The quantitative agreement is again fairly good.

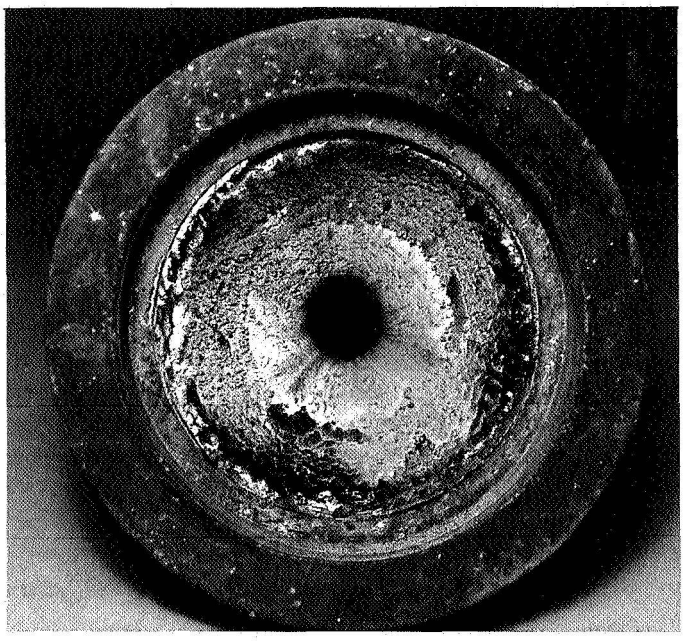

Fig. 10. Photograph of nozzle entrance surface showing erosion of the deposited layer of aluminum oxide

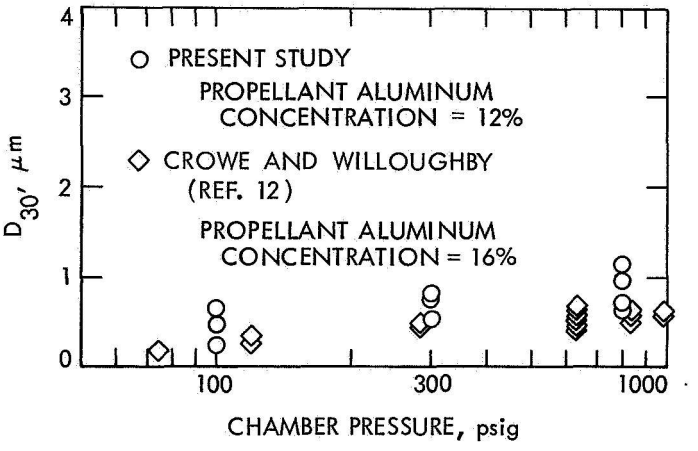

Fig. 11. Comparison of D_{30} from present study with data by Crowe and Willoughby (Ref. 12); latter data, reported as D_m, was converted to D_{30} as described

VII. Summary and Conclusions

A. Tank Collection Results

Tank collection tests of Al_2O_3 particles produced by a small rocket motor indicate that particle size is: (1) independent of receiver tank capacity, (2) independent of aluminum concentration within the propellant, and (3) weakly dependent on rocket motor chamber pressure;

i.e., size increases by a factor of 1.7 with a ten-fold increase in pressure. Spectrophotometric tests are in agreement with the last two of these three observations.

B. Spectrophotometric Tests

Spectrophotometric tests were conducted using transmission measurements at three wavelengths of light. The measurements can be interpreted with internal consistency by postulating that the size distribution function is bimodal. The small size spectrum is measured by wavelengths at $\lambda_1 = 0.365$ and $\lambda_2 = 1.01$ μm. The measured value is in agreement with the results of tank firings of rocket motors equipped with nozzles if the latter data is truncated to exclude the largest particles that appear in the discontinuous portion of the size spectrum.

C. Particle Growth by Velocity Slip and Collision

Based on the results of Item 1, we conclude that the low-moment ratios of the Al_2O_3 particles show no evidence of growth by velocity slip and collision during their passage through the rocket nozzle. We draw no conclusions on the possibility of growth of the high-moment ratios because the data on these ratios display very high scatter. The scatter is attributed to the extreme difficulty in sampling the large-size tail of the particle-size distribution function.

D. Data Comparison

Fairly good quantitative agreement exists between the data of Crowe and Willoughby for particle size of Al_2O_3 from motors without nozzles, the truncated tank collection data for motors with nozzles in the present study, and the data from spectrophotometric tests. These data together with various moment ratios given in column 3 of Table 5 are considered useful as values for the various mean sizes of the particles inside small rocket motors and at the nozzle entrance.

E. Large Particle Growth Mechanism

Evidence is presented that indicates that the Al_2O_3 deposited on rocket nozzle entrance and lateral surfaces is shed by aerodynamic erosion. We believe this to be a source of relatively large particles, which complicates interpretation of data based on high moment ratios.

F. Control of Large Particle Growth

The possibility of minimizing the production of particles formed by aerodynamic shedding of Al_2O_3 from the nozzle remains as a problem to be considered if sufficient interest exists in the future. Such a study could use nozzle designs intended to minimize or exaggerate shedding. Methods should be devised to allow separation of large and small particles to enable a more detailed study of selected portions of the particle size spectrum. One such method might be the systematic mixing, settling, and decanting in water in order to isolate the largest particles.

G. Motor Chamber Particle Growth Mechanisms

No evidence was found to indicate that the particle size of Al_2O_3 at the nozzle entrance could be controlled. It appears that the particle size at this point is influenced primarily by the gas phase and/or surface reactions that produce Al_2O_3 from the metallic specie and possible agglomeration mechanisms that operate in the region between the propellant surface and the nozzle entrance.

H. Exhaust Effluent Refractive Index

The impurities present in the primarily Al_2O_3 particulate effluent from the rocket motor control the coloration of the material. These impurities probably exert a dominant effect on the complex portion of the refractive index at high temperatures. The use of the complex portion of the refractive index measured for pure Al_2O_3 as representative of rocket motor particulate effluent in particulate radiant heat transfer calculations appears unjustifiable to the authors.

References

1. Dobbins, R. A., "Remote Size Measurements of Particulate Products of Heterogeneous Combustion," Eleventh Symposium (International) on Combustion, The Combustion Institute, p. 921, Aug. 1967.
2. Sehgal, R., *An Experimental Investigation of a Gas-Particle Flow System,* Technical Report 32-238. Jet Propulsion Laboratory, Pasadena, Calif., March 16, 1962.
3. Rannie, W. D., "Perturbation Analysis of One-Dimensional Heterogeneous Flow in Rocket Nozzles," *Progress in Astronautics and Rocketry,* Vol. 6, p. 117, Academic Press, 1962.
4. Dobbins, R. A., "Measurement of Mean Particle Size in a Gas-Particle Flow," *AIAA J.*, Vol. 1, p. 1940, 1963.
5. Dobbins, R. A., and Temkin, S., "Attenuation and Dispersion of Sound by Particulate Relaxation Processes," *J. Acoust. Soc. Am.*, Vol. 40, p. 317, 1966.
6. Marble, F. E., "Droplet Agglomeration in Rocket Nozzles Caused by Particle Slip and Collision," *Astronaut. Acta.*, Vol. 13, p. 159, 1967.
7. Mugele, R. A., and Evans, H. D., "Droplet Size Distribution in Sprays," *Ind. Eng. Chem.*, Vol. 42, p. 1317, 1951.
8. Kerr, P. L., *Optical Mineralogy,* Third Ed., p. 143, et seq., 1959.
9. Malitson, I. H., et al., "Refractive Index of Synthetic Sapphire," *J. Opt. Soc. Am.*, Vol. 48, p. 72, 1958.
10. Gryvnak, D. A., and Burch, D. E., "Optical and Infrared Properties of Al_2O_3 at Elevated Temperature," *J. Opt. Soc. Am.*, Vol. 55, p. 625, 1965.
11. Dobbins, R. A., and Jizmagian, G. S., "Optical Scattering Cross Sections for Polydispersions of Dielectric Spheres," *J. Opt. Soc. Am.*, Vol. 56, p. 1345, 1966.
12. Crowe, C. T., and Willoughby, P. G., "A study of Particle Growth in a Rocket Nozzle," *AIAA J.*, Vol. 5, p. 1300, 1967.
13. Rudinger, G., *Effective Drag Coefficients for Gas Particle Flow in Shock Tubes,* Project SQUID, Technical Report CAL-97-PU. Cornell Aeronautical Laboratory, Inc., Feb. 1969.
14. Selberg, B. P., and Nicholls, J. A., "Drag Coefficients of Small Spherical Particles," *AIAA J.*, Vol. 6, p. 401, 1968.